



HAL
open science

Toward the Mechanistic Understanding of Enzymatic CO₂ Reduction

Ana Rita Oliveira, Cristiano Mota, Cláudia Mourato, Renato M Domingos,
Marino Santos, Diana Gesto, Bruno Guigliarelli, Teresa Santos-Silva, Maria
João Romão, Inês Cardoso Pereira

► **To cite this version:**

Ana Rita Oliveira, Cristiano Mota, Cláudia Mourato, Renato M Domingos, Marino Santos, et al..
Toward the Mechanistic Understanding of Enzymatic CO₂ Reduction. ACS Catalysis, 2020, 10 (6),
pp.3844-3856. 10.1021/acscatal.0c00086 . hal-02938569

HAL Id: hal-02938569

<https://hal.science/hal-02938569>

Submitted on 18 Sep 2020

HAL is a multi-disciplinary open access archive for the deposit and dissemination of scientific research documents, whether they are published or not. The documents may come from teaching and research institutions in France or abroad, or from public or private research centers.

L'archive ouverte pluridisciplinaire **HAL**, est destinée au dépôt et à la diffusion de documents scientifiques de niveau recherche, publiés ou non, émanant des établissements d'enseignement et de recherche français ou étrangers, des laboratoires publics ou privés.

1 Toward the Mechanistic Understanding of Enzymatic CO₂ Reduction

2 Ana Rita Oliveira,^{||} Cristiano Mota,^{||} Cláudia Mourato, Renato M. Domingos, Marino F. A. Santos,
3 Diana Gesto, Bruno Guigliarelli, Teresa Santos-Silva, Maria João Romão,* and Inês A. Cardoso Pereira*



Cite This: <https://dx.doi.org/10.1021/acscatal.0c00086>



Read Online

ACCESS |



Metrics & More



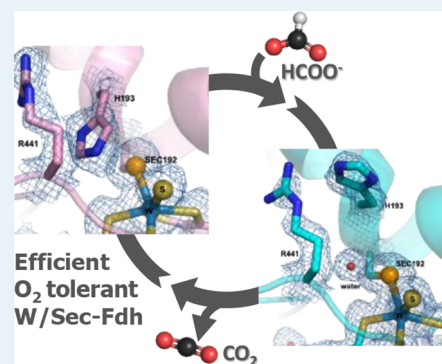
Article Recommendations



Supporting Information

4 **ABSTRACT:** Reducing CO₂ is a challenging chemical transformation that biology
5 solves easily, with high efficiency and specificity. In particular, formate dehydrogenases
6 are of great interest since they reduce CO₂ to formate, a valuable chemical fuel and
7 hydrogen storage compound. The metal-dependent formate dehydrogenases of
8 prokaryotes can show high activity for CO₂ reduction. Here, we report an expression
9 system to produce recombinant W/Sec-FdhAB from *Desulfovibrio vulgaris* Hilden-
10 borough fully loaded with cofactors, its catalytic characterization and crystal structures
11 in oxidized and reduced states. The enzyme has very high activity for CO₂ reduction
12 and displays remarkable oxygen stability. The crystal structure of the formate-reduced
13 enzyme shows Sec still coordinating the tungsten, supporting a mechanism of stable
14 metal coordination during catalysis. Comparison of the oxidized and reduced
15 structures shows significant changes close to the active site. The DvFdhAB is an
16 excellent model for studying catalytic CO₂ reduction and probing the mechanism of
17 this conversion.

18 **KEYWORDS:** formate dehydrogenase, CO₂ reduction, X-ray structure, oxygen-tolerance, tungsten, molybdopterin, moco



19 ■ INTRODUCTION

20 Developing sustainable processes to reduce the levels of
21 atmospheric CO₂ is one of the most urgent and difficult issues
22 facing our society. Converting CO₂ is a chemical challenge due
23 to its intrinsic kinetic and thermodynamic stability.^{1,2} Chemical
24 conversions require high energy inputs, have low selectivity, low
25 catalytic efficiencies, and often need rare-metal catalysts. This
26 contrasts with the high turnovers, high specificity, and mild
27 conditions observed in biology (through reductases, carbox-
28 ylases, and lyases).³ Studying the biochemical strategies, Nature
29 has developed to convert CO₂ is thus paramount to inspire
30 development of more selective, efficient, and sustainable
31 catalysts. CO₂ reduction to formate is the basis of the most
32 energy-efficient biological pathway of carbon fixation, the
33 reductive acetyl-CoA pathway,^{4,5} which is probably also the
34 most primordial form of carbon fixation.⁶ Technologically, this
35 reduction is of high interest as it allows CO₂ sequestration as a
36 valuable commodity chemical (formate), providing a means of
37 H₂ storage.^{7,8} Formic acid is a safe liquid, nontoxic and
38 nonflammable, with high volumetric energy density, and can
39 easily be transported. Direct formic acid fuels cells are already a
40 reality.⁸

41 In biology, CO₂ reduction to formate is performed by formate
42 dehydrogenases (FDHs). These enzymes are divided in two
43 classes: the metal-free, oxygen-tolerant, NAD⁺-dependent
44 enzymes present in plants, fungi, and some aerobic bacteria,
45 and the molybdenum- or tungsten-dependent enzymes present
46 in anaerobic prokaryotes.^{9–12} The metal-free, NAD⁺-dependent
47 enzymes are designed for formate oxidation (CO₂ reduction

from NADH is thermodynamically uphill), and are extremely
48 slow in the reductive direction. In contrast, both the Mo- and W-
49 dependent FDHs catalyze CO₂ reduction,^{13–16} even in the case
50 of the NAD(H)-dependent, multimeric Mo-FDHs.^{17,18} 51

52 In the metal-dependent FDHs, the active site consists of a
53 Mo/W atom coordinated by two Molybdopterin Guanine
54 Dinucleotides (MGD), one selenocysteine (Sec) or cysteine
55 residue and one terminal sulfido (=S/—SH) ligand. The
56 sulfido ligand is introduced by a dedicated chaperone and is
57 essential for activity.^{19–21} Despite considerable studies, the
58 mechanism used by FDHs to oxidize formate or reduce CO₂ is
59 still unclear. Several proposals have been made, and the topic has
60 raised considerable debate.^{11,12,22–24} Critical issues still under
61 discussion are (i) whether the Sec/Cys ligand dissociates from
62 the metal during catalysis and is replaced by formate,^{22,23,25–28}
63 or if metal coordination is maintained during catalysis;^{15,29,30}
64 and (ii) whether oxidation of formate involves hydride transfer
65 to the metal or sulfido group,^{15,26,29,30} or C_α proton abstraction
66 by a protein residue.^{28,31} A number of experimental and
67 computational tools have been explored to try to elucidate this
68 mechanism, namely X-ray crystallography,^{23,31–33} X-ray absorp-

Received: January 6, 2020

Revised: February 15, 2020

Published: February 27, 2020

tion spectroscopy,^{21,34,35} EPR,^{29,36–38} theoretical calculations,^{26,27,30} and inhibition studies.^{22,28,39} However, the results are not always conclusive due to the difficulty in confidently assigning the observations to relevant catalytic states, compounded by the intrinsic instability of the proteins, which may be present in inactivated states. There is, thus, an urgent need for detailed structural information on FDHs in different catalytic/redox states.

When focusing on CO₂ reduction to formate it seems logical to investigate FDHs that physiologically perform this function, rather than formate oxidation. This is the case of enzymes present in acetogens, which grow from converting CO₂ to acetate,⁴ in syntrophs, which produce formate and H₂ as vehicles for interspecies electron transfer,⁴⁰ and finally in the closely related sulfate reducing bacteria, which in the absence of sulfate also turn to a syntrophic lifestyle.⁴¹ In fact, the enzymes with the highest CO₂-reducing activities are all derived from these organisms, and include the hydrogen-dependent CO₂ reductases (HDRC) from the acetogens *Acetobacterium woodii* and *Thermoanaerobacter kivui*,^{14,16} the W-FDH from the syntroph *Syntrophobacter fumaroxidans*,^{13,42} and the Mo-FDH from the sulfate reducer *Desulfovibrio desulfuricans*.¹⁵

Here, we report a novel expression system for production of a W/Sec-FDH from *Desulfovibrio vulgaris* Hildenborough, DvFdhAB, and its catalytic and structural characterization. The DvFdhAB is responsible for CO₂ reduction in *D. vulgaris*⁴³ and is the main FDH expressed in this organism if tungsten is available,⁴⁴ revealing its physiological preference over the Mo-containing isoenzymes. In contrast to other high-activity FDHs containing W and Sec that need to be purified anaerobically,^{14,16,42} the DvFdhAB exhibits a remarkable oxygen tolerance, as it can be purified and handled aerobically. Its high activity, robustness, and simple composition make it an ideal model for biocatalytic applications. We report here the catalytic characterization of the DvFdhAB, inhibition studies and the crystal structures in the oxidized and reduced states. These results bring important information toward elucidating the catalytic mechanism of metal-dependent FDHs.

RESULTS

Expression System. Two different strategies were tested for production of recombinant DvFdhAB: tag-labeling of the *fdhA* gene (DVU0587), and complementation of a Δ *fdhAB* deletion mutant with an expression vector. For the first strategy, a suicide vector was constructed based on pMO719,⁴⁵ to directly modify *fdhA* in the genome (Figure S1A of the Supporting Information, SI). In the second approach, we used the *D. vulgaris* Hildenborough Δ *fdhAB* deletion strain,⁴³ for which a complementation vector, pRec-FdhAB-Strep was assembled (Figure S1B). The expression of FdhA was confirmed in both systems (Figure S2). The formate oxidation activity of the complemented strain was approximately three times higher than that of the genome-modified strain. Thus, DvFdhAB was routinely produced using the complementation strategy.

Purification and Activation Behavior. Both W and Sec-containing enzymes are catalytically more active than their Mo and Cys counterparts, but they usually suffer from being extremely oxygen-sensitive.⁴² Remarkably, the W/Sec-DvFdhAB could be purified and handled under aerobic conditions. Nitrate and glycerol were used as stabilizing agents. Nitrate is an inhibitor that helps to protect the enzyme,¹⁷ presumably by preventing loss of the labile sulfido group.^{29,46} As desired, a single affinity chromatography step was enough to

produce pure DvFdhAB (Figure S3). Identical reduction levels were obtained with formate as with dithionite (Figure S4), indicating that the enzyme is fully loaded with the tungsten-sulfido group (W=S/-SH), essential for reduction by formate.

Metal-dependent FDHs often require reductive activation to display maximal activity.^{15,47} In contrast to the *D. desulfuricans* Mo/Sec-FdhABC,¹⁵ a 30 min incubation with formate was not enough to fully activate DvFdhAB, as a significant lag phase was still observed (Figure S5). Preactivation for 30 min with both formate and DTT abolished this lag phase. Furthermore, just 5 min preincubation of DvFdhAB with 50 mM DTT (or TCEP) was enough to observe maximum initial activities, indicating full activation.

Enzyme Kinetics. DvFdhAB oxidizes formate with a turnover rate of $1310 \pm 50 \text{ s}^{-1}$ (Table 1). In contrast to a

Table 1. Kinetic Constants of *D. vulgaris* DvFdhAB

DvFdhAB	HCOO ⁻ oxidation	CO ₂ reduction
specific activity	$568 \pm 22 \text{ U mg}^{-1}$	$137 \pm 12 \text{ U mg}^{-1}$
turnover	$1310 \pm 50 \text{ s}^{-1}$	$315 \pm 28 \text{ s}^{-1}$
K_m	$16.9 \pm 2.8 \text{ } \mu\text{M}$	$420 \pm 47 \text{ } \mu\text{M (CO}_2\text{)}$

previous report⁴⁴ where DTT preactivation was not used, the DvFdhAB is in fact highly active in catalyzing CO₂ reduction with a turnover of $315 \pm 28 \text{ s}^{-1}$. This robust CO₂-reducing activity agrees with the fact that in vivo this enzyme is responsible for formate production, when W is available.⁴³ The activity of native DvFdhAB^{WT} was reevaluated in the new assay conditions, showing similar rates to the recombinant version: a turnover of $1104 \pm 62 \text{ s}^{-1}$ for formate oxidation, and of $304 \pm 41 \text{ s}^{-1}$ for CO₂ reduction. These high catalytic activities place the W/Sec-DvFdhAB among the most active CO₂ reductases yet reported.

The DvFdhAB pH optimum for formate oxidation is 7.6, but activity is sustained close to 80% between pH 7 and 10 (Figure 1). The pH optimum of the reductive reaction is 7.1, and the activity is held above 60% between pH 4.7 and 7.6. Due to the influence of carbonate on the pH (see SI text), the CO₂ concentration varies across the pH range. With 50 mM sodium bicarbonate as the CO₂ source the concentration of CO₂ (l) is only 3.6 mM at pH 7.5, and decreases drastically above that, to only 120 μM at pH 9. In addition, the ionic strength of the solution also increases at higher pHs, which may also have a detrimental effect on activity.¹⁸ These two factors likely explain the drastic drop in activity above pH 7. The kinetic constants were determined for both reactions at the pH optimum (Figure 1C/D, Table 1). The K_M for formate is $16.9 \pm 2.8 \text{ } \mu\text{M}$ at pH 7.6, which is in the same order of magnitude as *S. fumaroxidans* W-Fdhs,⁴² and significantly lower than the K_m of the *A. woodii* Mo-FdhF2 or *E. coli* Mo-FdhH, which are in the mM range.^{14,48} The K_M for CO₂ is $420 \pm 47 \text{ } \mu\text{M}$ (see SI text). The only FDH reported with higher CO₂ affinity is the *D. desulfuricans* Mo-FDH, with a K_m of $15.7 \text{ } \mu\text{M}$.¹⁵ However, this value was calculated by a linearized graphical method, which can introduce significant errors.

Inhibition by nitrate was tested, since this was used as stabilizing agent. DvFdhAB retains 40% of formate oxidation and 60% of CO₂ reduction activity in the presence of 100 mM nitrate, so this is a very weak inhibitor. Since the enzyme is diluted in the activity assays (at least 100 \times), the effect of nitrate in these assays will be negligible. Azide is a stronger inhibitor and at 10 mM it reduced the oxidative rate to only 7%, whereas about

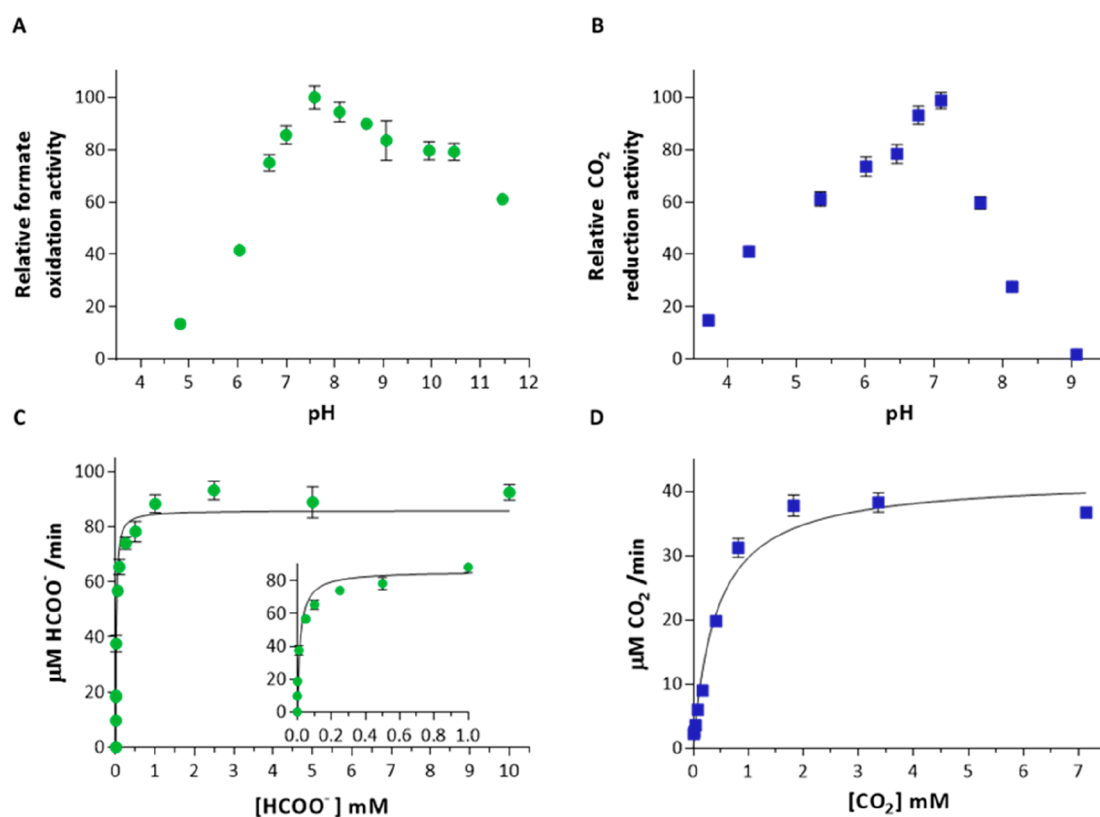


Figure 1. Kinetic characterization of DvFdhAB. (A) Effect of pH on formate oxidation activity (20 mM formate) and (B) on CO₂ reduction activity (with 50 mM sodium bicarbonate). (C) Steady-state formate oxidation kinetics and (D) steady-state CO₂ reduction kinetics. Lines represent the direct fitting of Michaelis–Menten equation to experimental data. All assays were performed in triplicate, and the error bars show the standard deviation.

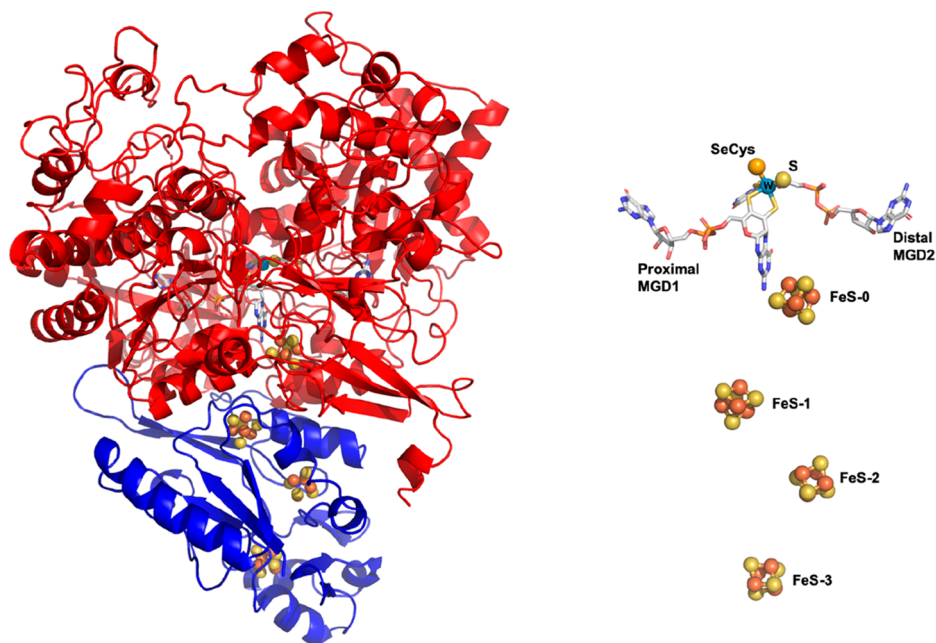


Figure 2. DvFdhAB structure. (Left) Structure of the heterodimer (α -subunit, red and β -subunit, blue). (Right) The metal cofactors, W(MGD)₂ and four [4Fe-4S] centers.

186 45% activity was sustained for CO₂ reduction. Thus, as reported
 187 for *E. coli* FdhH,²² the DvFdhAB is more strongly inhibited in
 188 the oxidized W(VI)=S than in the reduced W(IV)–SH state.
 189 We could not detect any activity for nitrate reduction, in contrast
 190 to the *R. capsulatus* enzyme.²⁸

Stability and Oxygen Tolerance. The stability of FDHs is 191
 critical for their use in biotechnological applications. DvFdhAB 192
 is quite thermostable, with a melting temperature of 77.3 ± 1.0 193
 $^{\circ}\text{C}$, which is increased to 79.8 ± 0.2 $^{\circ}\text{C}$ in the presence of nitrate 194
 and glycerol. Storage of the as-isolated pure DvFdhAB at 4 $^{\circ}\text{C}$ or 195

196 $-20\text{ }^{\circ}\text{C}$ in aerobic conditions did not lead to loss of activity even
 197 after 30 days (Figures S6 and S7). When kept aerobically at
 198 room temperature, the activity was stable for at least 10 h (Figure
 199 S8). However, when the enzyme was reduced by formate the
 200 activity was lost within 4 h of air exposure, and in the absence of
 201 nitrate and glycerol the loss occurred in less than 2 h. In contrast,
 202 under anaerobic conditions the formate-reduced enzyme
 203 maintains its activity even after 48 h (Figure S9). Overall, the
 204 oxidized enzyme is highly stable, which has already been
 205 exploited in semisynthetic systems for light-driven CO_2
 206 reduction.^{49,50}

207 **Crystal Structures in Oxidized and Formate-Reduced**
 208 **States.** For a mechanistic understanding of FDHs it is essential
 209 to have detailed structural information. There are only a few
 210 reported structures, from *E. coli* FdhH^{23,31} (EcFdhH), *E. coli*
 211 FdhN³² (EcFdhN), and *Desulfovibrio gigas* FdhAB
 212 (DgFdhAB),³³ and only one of these is from a reduced state
 213 (EcFdhH).³¹ This structure was later reinterpreted²³ revealing,
 214 unexpectedly, the dissociation of Sec from metal coordination,
 215 and the possible presence of mixed states at the active site. It is
 216 thus essential to get additional crystal structures of FDHs,
 217 particularly in the reduced state. The DvFdhAB was crystallized
 218 aerobically (oxidized form), as well as in an anaerobic chamber
 219 in the presence of formate (reduced form). The crystals of the
 220 oxidized form (DvFdhAB_{ox}, 6SDR) diffracted beyond $2.1\text{ }\text{\AA}$
 221 (Table S2), and the structure was solved by molecular
 222 replacement, using the *D. gigas* FdhAB structure³³ as the search
 223 model. The model was traced and refined to final crystallo-
 224 graphic R_{work} and R_{free} values of 18.6% and 22.6%, respectively,
 225 with good geometry. Crystals of the formate-reduced form
 226 (DvFdhAB_{red}, 6SDV) diffracted beyond $1.9\text{ }\text{\AA}$, and the
 227 structure was solved by molecular replacement using the
 228 oxidized form as search model. The model was refined to final
 229 crystallographic R_{work} and R_{free} values of 15.9% and 19.7%,
 230 respectively, with good geometry (Table S2).

231 The DvFdhAB is a heterodimer (Figure 2) and can be divided
 232 into four (FdhA) plus three (FdhB) domains (Figure S10),
 233 following the classification of DgFdhAB. The large, catalytic α
 234 subunit harbors the [W(MGD)₂, SH, Sec] cofactor and one
 235 [4Fe-4S] cluster, while the small β subunit contains three [4Fe-
 236 4S] clusters. The overall structure of the catalytic subunit is very
 237 similar to those of DgFdhAB and EcFdhN, with RMSDs of 1.30
 238 \AA for 957 α -carbons and $2.01\text{ }\text{\AA}$ for 947 α -carbons, respectively.
 239 As in other enzymes from the DMSO reductase family, the
 240 W(MGD)₂ cofactor is deeply buried inside the protein and
 241 stabilized by an extensive network of hydrogen bonding and
 242 hydrophobic interactions. The proximal MGD1 interacts with
 243 domains II and IV and is the only one involved in electron
 244 transfer. The closest pathway is via the exocyclic NH_2 of the
 245 pterin and the FeS-0 center, mediated by the N^{ϵ} of highly
 246 conserved Lys90. The distal MGD2 interacts with domains II
 247 and IV and is very likely involved in modulating the redox
 248 potential of the metal (see below).

249 The electron transfer β -subunit holds three [4Fe-4S] clusters
 250 and interacts with the large subunit covering a surface of ca. 2066
 251 \AA^2 (PDBePISA protein-protein interaction server; [http://](http://www.ebi.ac.uk/msd-srv/prot_int/)
 252 www.ebi.ac.uk/msd-srv/prot_int/). Several hydrophobic inter-
 253 actions, salt bridges, hydrogen bonds, and tightly bound water
 254 molecules stabilize the interface between the two subunits. This
 255 interaction involves over 60 residues of domains I, II, III, and IV
 256 in the large subunit and 50 amino acids in the small subunit. The
 257 overall structure of the β -subunit is very similar to those of
 258 DgFdhAB and EcFdhN, with rmsds of $1.08\text{ }\text{\AA}$ for 215 α -carbons

and $2.35\text{ }\text{\AA}$ for 208 α -carbons, respectively. The major difference
 259 is observed in loop 58–66 in DvFdhAB that is one residue
 260 longer than that in DgFdhAB, and is involved in an additional
 261 hydrophobic interaction with the α -subunit.
 262

Active Site in Oxidized and Reduced Forms. The
 263 DvFdhAB catalytic pocket and respective entrance tunnel is
 264 positively charged, and three glycerol molecules are modeled in
 265 this cleft (Figure 3). The glycerol closest to the W is hydrogen
 266

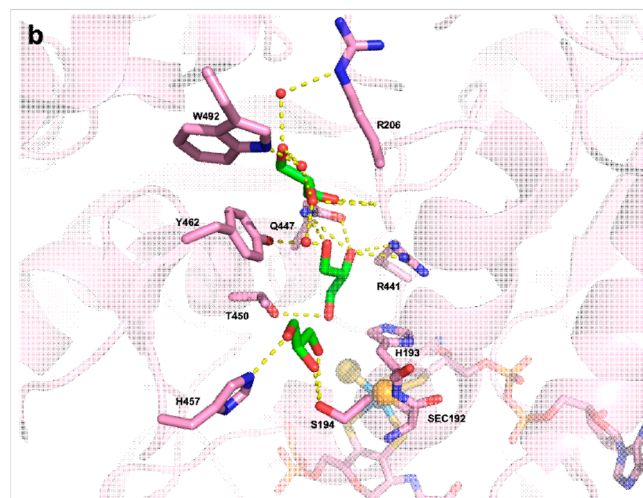
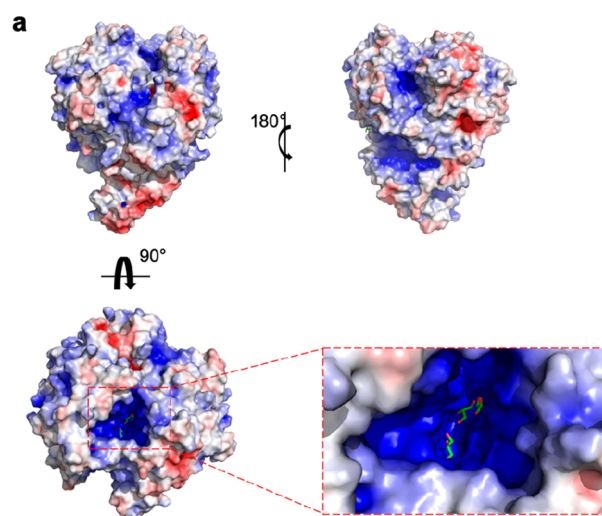


Figure 3. Protein surface charges and active site cavity. (a) Electrostatic potential mapping on DvFdhAB surface and active site pocket (oxidized form). The electrostatic potential was calculated using PyMOL's APBS plugin. Electropositive regions are colored blue, electronegative regions are colored red, and regions of neutral charge are colored white. Three glycerol molecules (green) were modeled in the tunnel leading to the catalytic pocket. (b) Detail of the substrate tunnel and active site, showing the interactions of the three glycerol molecules.

267 bonded by Ser194 and His457, the second glycerol is oriented
 268 by Arg441, Thr450, and a water molecule oriented by Tyr462.
 269 The third glycerol is found in the tunnel entrance, oriented by
 270 Gly207 backbone nitrogen and water molecules that make
 271 bridges with Trp492 and Arg206. These glycerol molecules
 272 probably mimic transit formate binding sites and shed light on
 273 the formate entrance/release mechanism.

The W center is fully loaded with metal (Figure S11)
 274 according to the relative B factors for a full occupancy of all
 275

276 atoms (Table S2), and is buried 30 Å away from the protein
 277 surface. In the oxidized form (DvFdhAB_ox), the metal is
 278 hexacoordinated to four sulfur atoms from the two dithiolenes, a
 279 selenium from Sec192 and a sulfur ligand (W-SH/≡S), in a
 280 distorted octahedral geometry (Figure 4a and S11). In the
 281 vicinity of the metal there are two strictly conserved amino acids,
 282 His193, establishing a π interaction with the Se from Sec192,
 283 and Arg441, which establishes a hydrogen bond with one of the
 284 glycerol molecules, and has been proposed to be responsible for
 285 orienting the substrate molecule.²³

286 In the formate-reduced form (DvFdhAB_red), the environ-
 287 ment surrounding the active site suffers a conformational
 288 rearrangement (Figure 4b,c). The Sec192 loop (Ile191-His193)
 289 suffers a distortion, and the Sec192 C α atom shifts up to 1.00 Å
 290 from the position occupied in the oxidized form. Part of an
 291 adjacent α -helix (Ser194-Pro198) is also displaced up to 2.25 Å
 292 (Thr196^{ox}-Thr196^{red}, C α -C α distance; not shown on figure
 293 for clarity). However, Sec192 remains coordinated to the metal
 294 (Figure S11b). Remarkably, the catalytically relevant His193
 295 moves away from the active site adopting a different rotamer,
 296 and a water molecule occupies the previous position of the
 297 imidazole ring, 3.18 Å away from Se, establishing a hydrogen
 298 bond with Gly442 amide bond. In addition, Arg441 side chain
 299 also suffers a small rearrangement. The Sec192 loop shift is
 300 propagated to neighboring amino acids from different domains
 301 with the consequent displacement of the adjacent hydrophobic
 302 Ile191 that promotes the tilt of the side chains of Trp533,
 303 Phe537, and Phe160.

304 To further confirm the W redox state in the formate-reduced
 305 crystals, we performed EPR spectroscopy on a sample prepared
 306 with small crystals spread in cryoprotectant solution, in parallel
 307 with a dissolved sample. Due to the random orientation of
 308 crystals in the polycrystal sample, the EPR spectrum can be
 309 directly compared to that given by a frozen solution.⁵¹ At 15 K
 310 the EPR spectra showed the [4Fe-4S]⁺²⁺ clusters of both
 311 samples in a fully reduced state (Figure S12). These signals
 312 broaden above 50 K and are no longer detected at 80 K. At this
 313 temperature no slow relaxing W(V) signal is detected in either
 314 sample, confirming that formate leads to full reduction of the
 315 protein to the W(IV) state, which is EPR silent. Very weak
 316 features are observed between $g = 1.92$ and 1.89 at $T = 80$ K but
 317 they cannot be assigned to a minor proportion of W(V) species.

318 Finally, conformational changes are also observed for the two
 319 MGDs cofactors and surrounding environment, which are more
 320 pronounced for the distal MGD2. In the oxidized form, Gln890
 321 is in close contact to MGD1, via a hydrogen bond to N5 of the
 322 piperazine central ring (assuming a tetrahydro form, Figure 4a).
 323 Additionally, Gln890 NH₂ is a H-bond donor to one of the
 324 dithiolene sulfur atoms and to the carboxylate of Glu443 (Figure
 325 S13). In the reduced form, Gln890 adopts a new rotamer and
 326 establishes a hydrogen bond to Glu443, which also adopts a
 327 different conformation (Figure S13). The interaction with the
 328 dithiolene sulfur atom is maintained. In contrast, the Gln890
 329 C=O group is now stabilized by an interaction to a water
 330 molecule present only in the reduced structure (Figures 4b and
 331 S13). This water molecule is hydrogen bonded to O1A, OS', and
 332 O4' from the dinucleotide part of MGD2. All these movements
 333 seem to promote a major distortion of the ribose moiety. Gln890
 334 and Glu443 are conserved in sulfate reducers, and in the
 335 DgFdhAB_ox structure their positions are conserved. A similar
 336 situation is observed in arsenite oxidase where a corresponding
 337 Gln is also interacting with N5 of the MGD1 pterin.⁵² In other
 338 reported FDH structures that glutamine residue is replaced by a

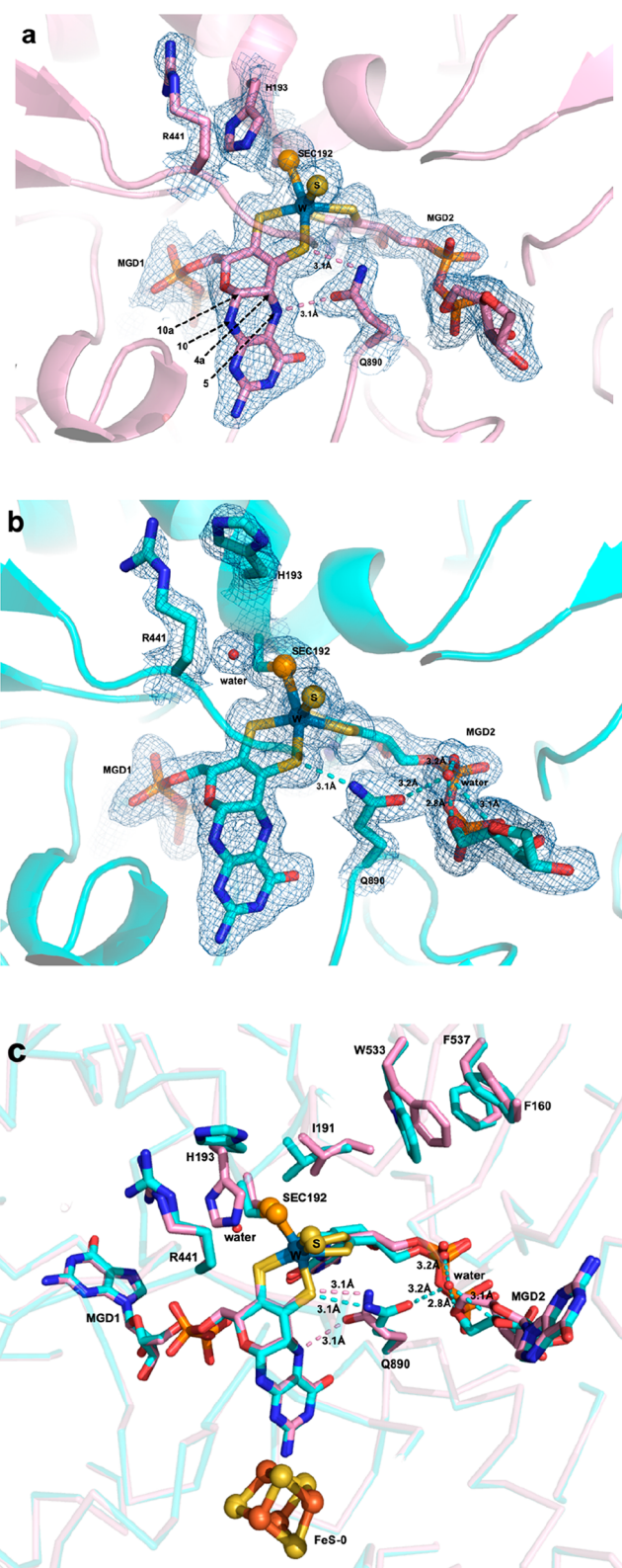


Figure 4. DvFdhAB active site. (a) Close-up view of the DvFdhAB_ox active site and 2Fo-Fc electron density map contoured at 1 σ ; (b) close-up view of the DvFdhAB_red active site and 2Fo-Fc electron density map contoured at 1 σ . (c) Superposition of the active sites of oxidized (pink) and reduced (cyan) forms.

Ser (EcFdhH) and by a His (EcFdhN and EcNarG⁵³). Rothery³³⁹ and co-workers assigned a “bridging” role to this residue (Gln, 340 Ser or His) providing H-bond interconnection between both 341

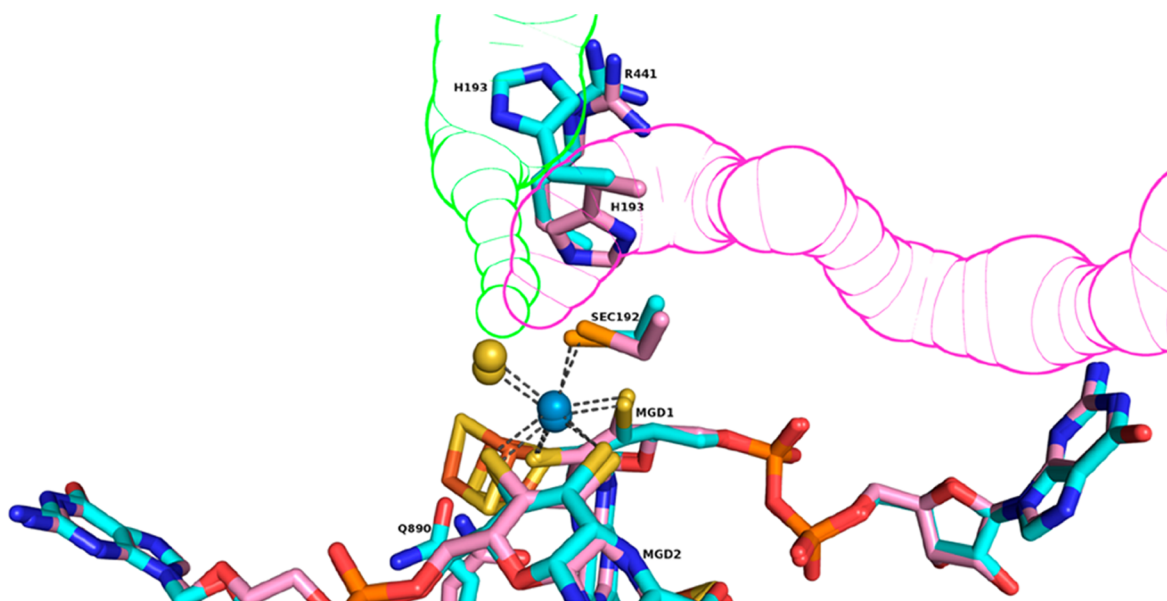


Figure 5. Proposed formate and CO₂ tunnels. The formate tunnel is represented in green and the CO₂ tunnel is represented in magenta. The imidazole ring of His193 is shown in pink (oxidized form) and in cyan (reduced form).

pyranopterins.⁵⁴ In these structures (EcFdhH ox and red) the “bridging” residue Ser587 also changes its rotamer but the smaller side chain precludes a close interaction to the MGD1 pterin.

Formate and CO₂ Tunnels. The tunnel network within the catalytic subunit was inspected with CAVER for both oxidized and reduced structures. In the oxidized form, the calculated tunnel with highest score links the positively charged funnel to the active site, assigned as the formate tunnel (Figure S14a), with a minimal diameter of 1.4 Å and a length of 13.2 Å. Strikingly, the tunnel with the highest score for the reduced structure, assigned as the CO₂ tunnel, is different (Figure S14b). It displays a minimal diameter of 1.8 Å and length of 39.7 Å, and also links the W active site to the protein surface. The surface of this tunnel is mainly composed by hydrophobic amino acids, and therefore it is likely to allow the access/release of nonpolar molecules such as CO₂. As discussed above, the imidazole ring of the conserved active site His193 is in a different position in oxidized and reduced structures. In the oxidized form its position closes the hydrophobic CO₂ tunnel, while in the reduced form His193 flips toward the formate tunnel opening the hydrophobic one and blocking the entrance of new formate molecules (Figure 5). Thus, the formate and CO₂ tunnels seem to be mutually exclusive, with His193 acting as a switch between the two.

The predicted tunnels are supported by analysis of amino acid conservation among the group of periplasmic NAD⁺-independent FDHs (which are phylogenetically separate from the cytoplasmic ones)⁵⁵ (Figure S15). The positively charged tunnel, for formate access/release, is composed by amino acids that present a high degree of conservation (at least 70% identity), whereas the hydrophobic tunnel presents a lower degree of conservation.

Inhibition by Iodoacetamide. Previous reports of Sec/Cys alkylation by IAA in *E. coli* FdhH³⁹ and the *R. capsulatus* Mo-Fdh²⁸ were taken as indication that the Sec/Cys residue dissociates during catalysis. Since the DvFdhAB_{red} structure indicates that Sec remains bound to W in this state, we tested the effect of iodoacetamide (IAA) alkylation on the activity.

Incubation of DvFdhAB with IAA at pH 7.6 resulted in 75% inhibition of the formate oxidation activity (Figure 6). Contrary

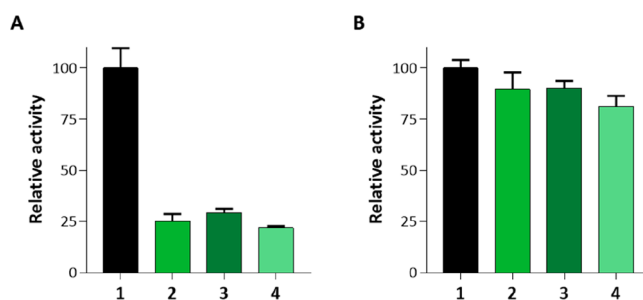


Figure 6. Inhibition by iodoacetamide. Formate oxidation activities after 30 min incubation without IAA (1), with 20 mM IAA (2), with 20 mM IAA and 20 mM formate (3), and with 20 mM IAA and 20 mM Nitrate (4) at pH 7.6 (A) and pH 9 (B). The activities were normalized to (1).

to *E. coli* FdhH³⁹ and *R. capsulatus* Mo-FDH,²⁸ this inhibition was not dependent on the presence of substrate. At pH 9, the IAA inhibition is considerably lower, but also no effect of substrate or inhibitor was observed. The IAA-treated samples were analyzed by mass spectrometry to reveal which residues were alkylated (Table S3). In all samples nine Cys are always alkylated (seven Cys coordinating FeS clusters, and two near the protein surface), which explains the inhibition observed. A peptide containing the IAA-alkylated Sec192 was not detected in any of the samples. Instead, all of the samples contained a peptide where Sec is modified to dehydroalanine. This modification is frequently identified in Sec-containing peptides, resulting from the loss of selenium during the MS sample preparation and analysis.^{56,57} If IAA-alkylation of Sec had happened, then this would prevent loss of selenium and the alkylated peptide would be easily identified.⁵⁶ This result suggests that the selenol ligand of DvFdhAB is not accessible for reaction with IAA, confirming the structural observations.

401 ■ DISCUSSION

402 CO₂ reduction by FDHs can vary by orders of magnitude, and in
403 the metal-dependent enzymes is often extremely oxygen
404 sensitive. The metal at the active site is one important
405 determinant for the level of this activity. Although the chemistry
406 performed by Mo is similar to that of W, W(IV) is a stronger
407 reductant than Mo(IV), and this is likely one of the reasons for
408 the higher reductive catalytic efficiency of W-FDHs. Another
409 important determinant is the presence of Sec versus Cys as
410 metal-coordinating residue. In *E. coli* FdhH a Sec/Cys variant
411 showed more than 2 orders of magnitude lower turnover than
412 the native enzyme, and was suggested to be directly involved in
413 the reaction.³⁹ A similar effect has been observed for a Sec/Cys
414 variant of the *D. vulgaris* Hildenborough [NiFeSe] hydrogenase,
415 where the Sec was additionally shown to be essential for the
416 oxygen tolerance of the enzyme.⁵⁸

417 The homologous expression system reported here allows
418 production of high levels of the W/Sec-DvFdhAB fully loaded
419 with cofactors. The simple composition of this enzyme, coupled
420 with its high activity and high stability, enabling aerobic
421 handling, make this enzyme an ideal model system for catalytic
422 and mechanistic studies of CO₂ reduction. In fact, the enzyme
423 has recently been explored for photocatalytic CO₂ reduction
424 coupled to Photosystem II,⁴⁹ or dye-sensitized TiO₂⁵⁰ in the first
425 report of visible light-driven CO₂ reduction without redox
426 mediators.

427 The W/Sec-DvFdhAB is among the most active enzymes for
428 CO₂ reduction. These include the trimeric W/Sec-Fdh1 from
429 the syntroph and sulfate reducer *S. fumaroxidans*. Its turnover
430 for CO₂ reduction was initially reported as 2460 s⁻¹,⁴² but was
431 later reevaluated to 282 s⁻¹.¹³ This enzyme is highly oxygen-
432 sensitive, requiring anaerobic isolation. Another example is the
433 Hydrogen-Dependent Carbon dioxide Reductase (HDCR)
434 from *A. woodii* that uses molecular hydrogen for the reduction
435 of CO₂.¹⁴ This multisubunit complex comprises one [FeFe]-
436 hydrogenase, two electron transfer subunits and a Mo/Sec-FDH
437 (FdhF2). The hydrogenation of CO₂ is catalyzed by HDCR at a
438 rate of 28 s⁻¹, but the CO₂ reduction activity of FdhF2 from
439 MV⁺ is 372 s⁻¹, similar to DvFdhAB. An HDCR from the
440 thermophile *T. kivui*, containing a W/Cys-FDH displays even
441 higher activity for CO₂ hydrogenation at 60 °C (2657 s⁻¹),¹⁶ but
442 curiously a lower formate oxidation activity (1337 s⁻¹) than the
443 *A. woodii* enzyme (1690 s⁻¹). Again, this enzyme has to be
444 isolated and handled anaerobically, and despite its thermotol-
445 erance shows some stability issues. The trimeric *D. desulfuricans*
446 Mo/Sec-FdhABC can be isolated and handled aerobically, but
447 its CO₂ reduction activity (47 s⁻¹)¹⁵ is 1 order of magnitude
448 lower than that of DvFdhAB. Still, the activity of these enzymes
449 is much higher than those of the oxygen-tolerant NADH-
450 dependent enzymes, with the highest activities reported for the
451 *Rhodobacter capsulatus* (1.5 s⁻¹)¹⁷ and *Cupriavidus necator*
452 enzymes (11 s⁻¹).¹⁸ In this context, the W/Sec-DvFdhAB stands
453 out as a unique model system, combining high catalytic activity
454 with good stability, enabling aerobic handling.

455 The stability profile of DvFdhAB allowed the enzyme to be
456 crystallized in two different redox states. This has previously
457 been achieved only for *E. coli* FdhH,³¹ a cytoplasmic enzyme that
458 is part of the formate-hydrogen lyase (FHL) complex and which
459 belongs to a different phylogenetic group.⁵⁵ The structure of the
460 DvFdhA catalytic subunit is quite similar to that of the four
461 available FDH crystal structures (rmsd 1.90 Å all atoms), with
462 the largest differences found between DvFdhAB and *E. coli*

FdhH, which has an additional long C-terminus helix. The 463
active sites are also very conserved, independently of having W 464
or Mo. In all available crystal structures, the protein W/Mo 465
ligand is a Sec and the sixth ligand is a sulfur (although not 466
corrected in the PDB for earlier deposited structures, 1FDO and 467
1kQF, where an oxygen was proposed). The structural analysis 468
now reported also allowed identification of putative formate and 469
CO₂ tunnels, which will be probed in future studies using 470
variants. 471

The reanalysis of the *E. coli* FdhH reduced structure³¹ raised 472
important questions regarding the mechanism of FDHs.²³ This 473
reinterpretation of the original crystallographic data revealed 474
that Sec is not coordinating the Mo in the formate-reduced 475
structure and is found ~9 Å away. Nevertheless, the poor 476
electron density of the active site region suggests a possible 477
mixture of states, where some Sec-Mo coordination may still be 478
present.²³ This reinterpretation supports mechanisms that 479
propose Sec/Cys displacement from the metal coordination 480
during catalysis.^{22,23,25,27,28} In contrast, the structure of the 481
reduced DvFdhAB shows clearly that Sec remains bound to the 482
metal in this redox state, suggesting a model of stable metal 483
coordination during catalysis. Since all metal-dependent FDHs 484
are likely to follow identical mechanisms, the Sec-displacement 485
in reduced *E. coli* FdhH may be explained by corresponding to a 486
transient state, or to the capture of an unproductive form of the 487
enzyme due to labile metal coordination. Such labile 488
coordination is supported by the observation that Sec/Cys can 489
be alkylated with IAA in *E. coli* FdhH³⁹ and *R. capsulatus* Mo- 490
FDH,⁴⁸ but not in DvFdhAB. Nevertheless, it should be pointed 491
out that Sec/Cys alkylation by IAA may also occur even when 492
metal coordination is maintained.⁵⁹ If the metal-Sec/Cys bond 493
is indeed labile in some enzymes, then it remains to be 494
determined whether this has mechanistic implications or is just 495
incidental. 496

Other relevant changes are observed when comparing the 497
DvFdhAB oxidized and reduced structures. In particular, there is 498
a pronounced movement of conserved His193, together with a 499
nearby helix and some aromatic residues close to the active site, 500
which is likely to be mechanistically relevant. This is 501
accompanied by a conformational change of the distal MGD2 502
(also observed in reduced EcFdhH), which agrees with the 503
proposal that pyranopterins are noninnocent ligands, being 504
probably involved in redox tuning of the metal.^{54,60–62} 505
Comparing the MGD cofactors in the structures of FDHs and 506
nitrate reductases, there is a remarkable superposition of MGD1, 507
involved in the electron transfer pathway (Figure S16). The 508
contact of MGD1 with the FeS-0 center is mediated by a highly 509
conserved lysine (Lys90 in DvFdhAB), which establishes a 510
hydrogen bond with the exocyclic NH₂ of the pyranopterin. This 511
conserved pathway is present both in FDHs and in the related 512
nitrate reductases.⁶³ In contrast, the orientation and geometry of 513
the distal MGD2 varies considerably among the homologous 514
enzymes. These differences are accompanied by changes in the 515
orientation of amino acid side chains that surround the extended 516
cofactor. When comparing the DvFdhAB oxidized and reduced 517
forms, the reorientation of the “bridging” Gln890 is noteworthy, 518
suggesting a putative change in the redox state of the proximal 519
pterin. Rothery et al. analyzed the conformations of 319 520
pyranopterins in 102 protein structures and concluded that the 521
electron-transfer MGD1 pyranopterin is in a tetrahydro 522
oxidation state.⁶⁰ However, we consider that a mixture of 523
pyranopterin redox states cannot be excluded. Interestingly, for 524
arsenite oxidase the replacement of the structurally equivalent 525

Gln residue to a Gly stabilized a Mo(V) state.⁵² The same was reported for *E. coli* Nar,⁵³ where substitution of His1098 (corresponding to Gln890) by an Ala also increased the stability of the Mo(V) state. The structural changes observed in DvFdhAB together with mutagenesis data on other DMSOR family enzymes are congruent in showing the importance of the H-bond interactions bridging both pyranopterins in controlling the active site redox chemistry and catalysis. Although very high resolution (<1.5 Å) is required to assign the correct redox state to each pyranopterin, these observations raise the important point that computational predictions of enzymatic mechanisms should take into account also the putative redox role of the MGD cofactors.

CONCLUSIONS

In summary, we show that the recombinant DvFdhAB is a stable, highly active model system for CO₂ reduction. The structures reported here suggest that Sec remains bound to the metal during the catalytic cycle but clear changes in the second coordination sphere and in pyranopterin stabilization occur in the reduced enzyme. These changes include different H-bonding interactions between surrounding amino acids and both pyranopterins, agreeing with previous reports on the role of the pyranopterin in fine-tuning the metal redox potential and enzymatic activity. Our combined results do not support a mechanism of Sec/Cys dissociation from the metal, and agree with a second coordination sphere mechanism that may involve hydride transfer. Nevertheless, more detailed studies with future variants and new crystal structures will be required to allow further detailed insights into the catalytic mechanism, and production of improved engineered forms of this important enzyme.

MATERIALS AND METHODS

Expression of *fdhAB*. The vectors used for homologous expression and StrepII tag insertion of DvFdhAB were both constructed using the Sequence and Ligation Independent Cloning—SLIC—method, as described previously.⁵⁸ For the complementation vector plasmid pMO9075 was used as a source of the *Desulfovibrio* pBG1 replicon, the pUC origin of replication and the *aadA* gene, which confers resistance to spectinomycin – Sm^R. In this strategy the full *fdhA* gene, including the signal peptide sequence, and the C-terminal strepII tag, was introduced with the 21 bp ribosomal-binding site on the pMO9075 plasmid.⁴⁵ The primers were manufactured by Nzytech and are presented in Table S4. The fragments were treated separately with 0.5 U of T4 DNA polymerase (BioLabs Inc., New England), in the presence of 100 μg/mL of bovine serum albumin, for 60 min at room temperature, and the reaction was stopped by the addition of 1 mM dCTP. The treated fragments were mixed in a 1:1 molar ratio in T4 DNA ligase buffer (BioLabs Inc., New England) and incubated during 30 min at 37 °C. After a 10 min incubation on ice, 5 μL of the mixed fragments were transformed into 50 μL *E. coli* α-select Silver Efficiency (Bioline) and cells were plated on spectinomycin (100 μg/mL)-containing agar plates. The correct plasmid construct was screened by colony PCR and later confirmed by sequencing by GATC biotech, Germany.

For transformation, *D. vulgaris* and Δ*fdhAB* deletion strain were grown in MOY medium, with 30 mM sodium lactate/30 mM sodium sulfate (MOYLS) and 1.2 mM sodium thioglycolate. The constructed plasmids were then electro-

porated as previously described:⁴⁵ the suicide vector was electrotransformed with 1500 V, 250 Ω, and 25 μF on the wild-type strain to induce double recombination; the complementation vector was integrated in the Δ*fdhAB* deletion strain by electroporation with 1250 V, 250 Ω, and 25 μF (Gene Pulse Xcell, Bio-Rad). Transformed cells were left to recover overnight at 37 °C in 1 mL MOYLS medium and then plated inside the glovebox using MOYLS with 1.5% (w/v) agar, containing Geneticin G418 (400 μg/mL) and/or spectinomycin (100 μg/mL). Selected colonies were grown in liquid MOYLS and confirmed by PCR for *fdhB* gene. As a final confirmation, Strep-tagged DvFdhAB expression was verified by Western blot.

Organism and Growth Conditions. *D. vulgaris* Hildenborough (DSM 644) cells were grown in modified Postgate medium C containing 3.7 mM KH₂PO₄, 18.7 mM NH₄Cl, 17.6 mM Na₂SO₄, 0.4 mM CaCl₂·2H₂O, 0.24 mM MgSO₄·7H₂O, 1 g/L yeast extract, 26 μM FeSO₄·7H₂O, 1 mM sodium citrate tribasic dihydrate, 0.57 mM L-ascorbic acid, 0.88 mM sodium thioglycolate, 40 mM sodium formate, 10 mM sodium DL-lactate and 100 mM (12.1 g/L Tris base, supplemented with 1 μM of NiCl₂·6H₂O/Na₂SeO₃·5H₂O and 0.1 μM of Na₂O₄W·2H₂O. In the case of the Δ*fdhAB* complemented-strain, the concentration of Ni, Se, and W was increased to 10 μM. Moreover, to limit the concentration of Mo in the medium, the amount of yeast extract used was reduced to 0.4 g/L. Growth was performed at 37 °C in a 300 L reactor with N₂ atmosphere. Cells were recovered by centrifugation and stored at –80 °C.

Western Blot. Cells were disrupted using BugBuster Protein Extraction Reagent (Novagen, Inc.). The soluble fraction was run on a 12% SDS-polyacrylamide gel and transferred to a polyvinylidene difluoride—PVDF—membrane for 1 h at 350 mA and 4 °C in a Mini Trans-Blot electrophoretic transfer cell (Bio-Rad). Membranes were blocked using PBS buffer with 3% BSA and 0.5% (v/v) Tween 20, and then washed in PBS buffer with 0.1% (v/v) Tween 20. The membrane was incubated with biotin blocking buffer (IBA Lifesciences, Germany) and then treated with Strep-Tactin antibody labeled with alkaline phosphatase (IBA Lifesciences, Germany) diluted 1:4000. After washing, immunodetection of bound antibodies was done, in the dark, by membrane treatment with ready-made solutions of nitro-blue tetrazolium and 5-bromo-4-chloro-3'-indolylphosphate—NBT-BCIP (Sigma), in 100 mM Tris-HCl pH 8.0, 100 mM NaCl, and 5 mM MgCl₂ buffer. Reaction was stopped by washing the membrane with distilled water.

Protein Purification. For DvFdhAB^{WT} purification, cells were resuspended, in 20 mM Tris-HCl pH 7.6 and 10 mM NaNO₃ buffer, containing DNase, and disrupted in a French pressure cell in aerobic conditions. The crude extract was centrifuged at 8000g for 20 min at 4 °C, and the supernatant was further clarified by ultracentrifugation at 109 000g for 2 h at 4 °C. All the purification steps were performed at 4 °C aerobically. The soluble fraction was then loaded on a Q-sepharose high performance column, equilibrated with 20 mM Tris-HCl pH 7.6 with 10% (v/v) glycerol and 10 mM NaNO₃ (buffer A). Elution was carried out at a flow rate of 4 mL/min, with stepwise increments on NaCl concentration (50–200 mM steps, from 0 to 200 mM). The buffer of the fractions containing FDH activity (eluted around 150 mM NaCl) was exchanged to 20 mM KPi (K₂HPO₄/KH₂PO₄) buffer also with 10% (v/v) glycerol, and 10 mM NaNO₃ (buffer K), using a 30-kDa cutoff ultracentrifugation unit (Amicon Ultra-15 30K NMWL, Millipore). Then, 15% (v/v) (NH₄)₂SO₄ was added to the sample, which was further purified using a phenyl sepharose high performance column 648

649 equilibrated with buffer K with 15% (v/v) $(\text{NH}_4)_2\text{SO}_4$. Elution
650 was performed by reducing the ionic strength in a stepwise
651 decreasing gradient with a flow rate of 2 mL/min. Pure
652 DvFdhAB was eluted between 10.5 and 12% (v/v) $(\text{NH}_4)_2\text{SO}_4$,
653 and the purity of the eluted fractions was evaluated by 12% SDS-
654 polyacrylamide gel stained with Coomassie Brilliant Blue R-250.

655 For recombinant DvFdhAB affinity purification, cells were
656 resuspended in 100 mM Tris-HCl pH 8.0 with 10% (v/v)
657 glycerol, 10 mM NaNO_3 , and 150 mM NaCl (buffer W). Cell
658 disruption and soluble fraction clarification were performed as
659 described above. The soluble fraction was then directly loaded
660 on a Strep-tactin gravity flow (IBA Lifesciences, Germany)
661 column equilibrated with buffer W. After five washing steps with
662 buffer W, the recombinant protein was eluted with buffer W plus
663 2.5 mM D-desthiobiotin. The buffer of eluted samples was
664 exchanged to buffer A and samples were stored, under nitrogen
665 atmosphere, at 4 °C for immediate use, or -80 °C for longer
666 periods. This column yields pure DvFdhAB as judged by 10%
667 SDS-polyacrylamide gel.

668 Protein concentration was measured with the BCA Protein
669 Assay Kit from Novagen, with bovine serum albumin as
670 standard. The UV-visible absorption spectra of high purity
671 oxidized sample was acquired on a UV-1800 Shimadzu
672 spectrophotometer, and used to determine the molar extension
673 coefficient. The UV-visible spectrum was also recorded for
674 DvFdhAB after reduction with 20 mM formate, for 30 min, and
675 with 1 mM dithionite, inside the glovebox. Routine UV-visible
676 absorption spectra were obtained with a Nanodrop ND2000C.
677 The molar extinction coefficient of the oxidized enzyme at 410
678 nm, was determined to be $\epsilon_{410\text{ nm}} = 43\,446\text{ M}^{-1}\text{ cm}^{-1}$.

679 **Thermal Shift Assay.** The melting temperature of
680 DvFdhAB was determined using the Applied Biosystems
681 Protein Thermal Shift Dye Kit: 1 to 2 mg/mL of pure enzyme,
682 in buffer A or buffer T (20 mM Tris-HCl pH 7.6), was mixed
683 with the dye (2–6× fold) and the melting curve recorded from
684 25 to 99 °C, on the QuantStudio 7 Flex Real-time PCR System
685 from Applied Biosystems.

686 **Activity Assays and Kinetic Analysis.** Activity assays were
687 performed with small adaptations from previously reported
688 protocols.^{42,43} FDH activity was determined using a UV-1800
689 Shimadzu spectrophotometer, inside a COY Anaerobic
690 chamber, with an atmosphere of 2% H_2 /98% N_2 , at room
691 temperature, with stirring. During assay optimization, different
692 preincubations, their time, order of additions, and concen-
693 trations were tested. In the optimized method, the enzyme
694 sample was preincubated with 50 mM DTT for 5 min prior to
695 the reaction. Routinely, for formate oxidation measurements the
696 reduction of 2 mM benzyl viologen was monitored at 555 nm
697 ($\epsilon_{555\text{ nm}}(\text{BV}^+) = 12\text{ mM}^{-1}\text{ cm}^{-1}$), in 50 mM KPi pH 7.6
698 containing 1 mM DTT plus 20 mM sodium formate. One unit of
699 oxidizing activity is defined as the amount of FDH capable of
700 oxidizing 1 μmol of formate (reducing of 2 μmol of BV^{2+}) per
701 min. For the reduction of CO_2 , Zn-reduced methyl viologen was
702 used as artificial electron donor. The oxidation of MV^+ (0.1
703 mM) was followed at 578 nm ($\epsilon_{578\text{ nm}}(\text{MV}^+) = 9.7\text{ mM}^{-1}$
704 cm^{-1}), in 50 mM KPi pH 6.9 with 1 mM DTT plus 50 mM
705 sodium bicarbonate, as a source of CO_2 (after the addition of
706 bicarbonate the pH rises to approximately 7.1). One unit of
707 reducing activity is defined as the amount of FDH capable of
708 reducing 1 μmol of CO_2 (oxidizing 2 μmol MV^+) per min. In
709 assays with pure DvFdhAB a final concentration of 1.4 nM
710 enzyme was used. The turnover numbers were calculated
711 considering one catalytic active protomer $\alpha\beta$ (138 kDa). To

evaluate inhibition by nitrate and azide, measurements were
712 performed in the presence of 100 mM of nitrate or 10 mM of
713 sodium azide. 714

The influence of pH on FDH activity was assessed using a
715 buffer mix containing 100 mM glycine, K_2HPO_4 , citric acid, and
716 Tris. The pH was adjusted using HCl or KOH. The activity of
717 the purified DvFdhAB was measured at substrate concentrations
718 ranging from 0.5 μM to 10 mM sodium formate, at the optimum
719 pH of 7.6. For the CO_2 reductase activity, concentrations of 75
720 μM to 50 mM sodium bicarbonate were employed at the
721 optimum pH of 7.1 (see SI). In these assays, sodium bicarbonate
722 was the last component to be added before starting the assay
723 with the enzyme. Kinetic parameters were calculated by direct
724 fitting of the Michaelis–Menten equation, using the least-
725 squares method, using Graph Pad Prism 7. 726

Iodoacetamide Assays. The effect of iodoacetamide (IAA)
727 was measured on the formate-oxidation activity. We could not
728 measure the IAA effect on CO_2 reduction because IAA oxidizes
729 MV^+ nonspecifically. As-isolated DvFdhAB was incubated for 30
730 min with 20 mM of IAA, alone or in the presence of 20 mM
731 formate, or 20 mM nitrate, in 20 mM Tris HCl pH 7.6, 10%
732 glycerol. After that, the IAA-treated samples were incubated for
733 5 min with DTT prior to measurement of formate oxidation
734 activities. 735

For mass spectrometry analysis, 10 μg of IAA-treated
736 DvFdhAB were digested with trypsin overnight at 37 °C. The
737 resulting peptides were analyzed by LC–MS, with data acquired
738 in positive TOF-MS mode using X500B QTOF (ABSciex) with
739 Turbo V ion source (Sciex) mass spectrometer connected to the
740 ExionLC AD UPLC system. External calibration was performed
741 using β -galactosidase digest (ABSciex). The raw MS and MS/
742 MS data were analyzed using the Explorer software of SCIEX
743 OS-Q, the BioPharmaView software 3.0 (Sciex) and the Protein
744 Pilot for peptide identification. Data were obtained by the Mass
745 Spectrometry Unit (UniMS), ITQB/iBET, Oeiras, Portugal. 746

**Crystallization, Data Collection, Structure Solution,
747 and Refinement.** For the crystallization of DvFdhAB, the
748 commercial screens JBS 1, 2, 3, and 4 (Jena Biosciences) were
749 used and 1 μL drops (1:1 protein:precipitant ratio) were
750 dispensed using an Oryx8 crystallization robot (Douglas
751 Instruments, Ltd.). The drops were set in 96 Well CrystalQuick
752 X Plates (Greiner Bio-One) using the sitting-drop vapor
753 diffusion method, and the plates were stored at 20 °C. 754

Thin needles appeared within 4 days on condition F11 (32%
755 PEG 3350, 0.1 M Tris-HCl pH 8.5, 0.8 M LiCl) and were tested
756 in situ using the home source (Bruker D8 Venture dual source
757 X-ray generator equipped with a Photon 100 CMOS detector
758 and the ISX stage). These crystals presented a protein diffraction
759 pattern with very weak spots. In order to improve crystal quality
760 and size, a scale up of the condition to 2 μL hanging drops was
761 performed, with 1:1 protein/precipitant ratio, and the
762 precipitant and salt concentrations were optimized. The best
763 crystals appeared after 24 h with 32% PEG 3350, 0.1 M Tris-HCl
764 pH 8.5, and 1 M LiCl. The crystals grew as thin plates to a
765 maximum size of $0.1 \times 0.2 \times 0.05\text{ mm}^3$ in 7 days. 766

The crystallization of DvFdhAB in the formate-reduced form
767 was performed in an anaerobic chamber under an argon
768 atmosphere at <0.1 ppm of oxygen, and all the solutions used
769 were previously degassed and stored in the anaerobic chamber.
770 The protein was incubated with 10 mM of sodium formate, and
771 the crystallization drops were prepared in the previously
772 optimized condition (32% PEG 3350, 0.1 M Tris-HCl pH 8.5,
773 1 M LiCl). Crystals of the reduced form appeared after 1 week
774

775 with the same shape of the oxidized form. The crystals were
776 transferred into a cryoprotectant solution consisting of reservoir
777 solution augmented with 20% (v/v) glycerol and then flash-
778 cooled in liquid nitrogen.

779 X-ray diffraction data sets were collected at 100 k using a
780 Pilatus 6M-F detectors on ID29⁶⁴ and ID30⁶⁴ beamlines at the
781 European Synchrotron Radiation Facility. The X-ray diffraction
782 images were integrated with XDS,⁶⁵ and data were scaled and
783 merged using CCP4 program Aimless.⁶⁶ The crystals of the
784 oxidized form (DvFdhAB_ox) belong to space group $P2_12_12_1$
785 with unit cell parameters $a = 64.59 \text{ \AA}$, $b = 127.64 \text{ \AA}$, and $c =$
786 148.21 \AA and diffracted beyond 2.1 \AA . The structure was solved
787 by molecular replacement with Phaser⁶⁷ using the structure of
788 formate dehydrogenase from *Desulfovibrio gigas* to build the
789 search model (PDB 1H0H). The two protein sequences share
790 around 64% identity, and the search model was prepared with
791 the CHAINSAW⁶⁸ tool from CCP4 software package, non-
792 conserved residues were pruned down to the γ -atom. Crystals of
793 the formate-reduced form (DvFdhAB_red) belong to the same
794 space group with almost identical unit cell parameters $a = 64.89$
795 \AA , $b = 128.56 \text{ \AA}$, and $c = 149.63 \text{ \AA}$ and diffracted beyond 1.9 \AA .
796 The structure was also solved by molecular replacement but
797 using the oxidized form as search model. Model building and
798 refinement were performed with Coot⁶⁹ and phenix.refine.⁷⁰
799 The refined models for oxidized and reduced forms (PDB
800 entries 6SDR and 6SDV) contain 1177 and 1181 amino acid
801 residues, respectively, and were assessed using Molprobrity
802 (Table S2). Data processing and refinement statistics are
803 presented in Table S2.

804 **Tunnel Calculation.** The program CAVER 3.0.1 was used
805 as a PyMOL plugin⁷¹ for calculating the tunnels in DvFdhAB,
806 using manually adjusted settings. The initial starting point (S
807 atom from W-SH), shell depth (2 \AA), shell radius (3 \AA), cluster
808 threshold (3.5 \AA), desired radius (5 \AA), and maximum distance
809 (3 \AA) were maintained constant for all calculations. The
810 maximum distance specifies the furthest point (from the initial
811 point) to start a tunnel calculation. The bottleneck radius is the
812 narrowest part of a given tunnel and corresponds to the
813 minimum probe radius. The tunnel analysis provided a list of
814 calculated tunnels that were ranked according to a specific cost
815 function (e.g., for two tunnels with equal radii, the one with the
816 shorter distances has a lower cost). The tunnel with the lowest
817 cost was chosen as the primary tunnel.

818 **Sequence Analyses.** The amino acid sequence of *D.*
819 *vulgaris* FdhA (UniProt- Q72EJ1) was used as query search
820 against the UniProt reference proteomes via the Hidden Markov
821 Model (HMM) profile implemented in the Phmmer web
822 server.⁷² The search was performed using default parameters
823 and 6063 sequences were found (June 2019), which include a
824 range of different Mo/W oxidoreductases. These sequences
825 were subjected to multistep clustering based on sequence
826 identity at 95% (5848 clusters), 75% identity (2599 clusters),
827 and 50% identity (608 clusters), using the h-CD-HIT software
828 present in the CD-HIT web suite.⁷³

829 A Maximum Likelihood (ML) phylogenetic tree was built
830 based on a multiple sequence alignment of the 608 sequences
831 representing each cluster, performed with the MAFFT
832 software⁷⁴ using default options. Fourteen well-known FDH
833 sequences were also included in the alignment (FdnG-1 and
834 FdnG-2 from *D. vulgaris*; FdhA from *D. gigas*; Dde_0717 from
835 *D. alaskensis*; Ddes_0555 from *D. desulfuricans*; Dret_0226 from
836 *D. retbaense*; Sfum_0036 and Sfum_3510 from *S. fumaroxidans*;
837 FdhA from *R. capsulatus*; FdnG from *C. necator*; FdhF from *T.*

kivui; FdhF-2 from *A. woodii*; and FdnG and FdhF from *E. coli*). 838
For inference and preparation of the phylogenetic tree, we used 839
the MEGA X 10.1 software with default parameters.⁷⁵ FdhA 840
proteins separate into two different branches in the phylogenetic 841
tree.⁵⁵ One representing periplasmic NAD-independent FdhAs 842
and containing 41 CD-HIT cluster representative sequences 843
plus 10 known sequences (where *D. vulgaris* FdhA and *E. coli* 844
FdhN and FdhO are included), and another representing 845
cytoplasmic NAD-dependent FdhAs and containing 35 CD- 846
HIT cluster representative sequences plus 4 known sequences 847
(including *E. coli* FdhH). The multiple sequence alignment was 848
edited using the Jalview software,⁷⁶ where gaps were trimmed 849
using *D. vulgaris* FdhA as reference. The consensus logo (Figure 850
S14) was created with Jalview, based on the alignment of the 51 851
sequences from the branch of NAD-independent FdhAs. 852

EPR Spectroscopy. EPR spectra were recorded at X-band 853
on a Bruker Elexsys 500 spectrometer equipped with an Oxford 854
Instruments ESR900 helium gas flow cryostat. Formate-reduced 855
crystals of DvFdhAB, prepared as described above, were 856
transferred to an EPR tube inside the glovebox (Jacomex). A 857
solution sample of DvFdhAB (100 μL of 162 μM in Buffer A) 858
was transferred to an EPR tube inside the glovebox and reduced 859
by adding 20 μL of 60 mM sodium formate to the protein 860
solution. EPR tubes were let to incubate for few minutes at room 861
temperature, capped, transferred out of the glovebox, and frozen 862
immediately in liquid nitrogen. 863

■ ASSOCIATED CONTENT

 864

SI Supporting Information

 865

This material is available free of charge on the ACS Publications 866
Web site. The Supporting Information is available free of charge 867
at <https://pubs.acs.org/doi/10.1021/acscatal.0c00086>. 868

Plasmid sequence maps; Western blot of DvFdhAB- 869
expressing strains; SDS-PAGE gel of purified DvFdhAB; 870
UV-visible spectrum of DvFdhAB; activity assays with 871
different activation protocols; stability assays in different 872
conditions; domains of DvFdhAB; electron density of 873
DvFdhAB active site; EPR spectra of formate-reduced 874
DvFdhAB in crystals and in solution; Gln890 environ- 875
ment in oxidized and reduced structures; formate and 876
 CO_2 tunnels; sequence conservation of residues lining the 877
formate and hydrophobic tunnels; structural alignment of 878
MGDs; calculations of dissolved CO_2 concentrations; 879
crystallographic data processing and refinement statistics; 880
reactivity of DvFdhAB cysteines with iodoacetamide; and 881
primers (PDF) 882

■ AUTHOR INFORMATION

 883

Corresponding Authors

 884

Maria João Romão – UCIBIO, Applied Molecular Biosciences 885
Unit, Departamento de Química, Faculdade de Ciências e 886
Tecnologia, Universidade Nova de Lisboa, 2829-516 Caparica, 887
Portugal; Email: mjr@fct.unl.pt 888

Inês A. Cardoso Pereira – Instituto de Tecnologia Química e 889
Biológica, Universidade Nova de Lisboa, 2780-157 Oeiras, 890
Portugal; orcid.org/0000-0003-3283-4520; 891
Email: ipereira@itqb.unl.pt 892

Authors

 893

Ana Rita Oliveira – Instituto de Tecnologia Química e Biológica, 894
Universidade Nova de Lisboa, 2780-157 Oeiras, Portugal 895

- 896 **Cristiano Mota** – UCIBIO, Applied Molecular Biosciences Unit,
897 Departamento de Química, Faculdade de Ciências e Tecnologia,
898 Universidade Nova de Lisboa, 2829-516 Caparica, Portugal
- 899 **Cláudia Mourato** – Instituto de Tecnologia Química e Biológica,
900 Universidade Nova de Lisboa, 2780-157 Oeiras, Portugal
- 901 **Renato M. Domingos** – Instituto de Tecnologia Química e
902 Biológica, Universidade Nova de Lisboa, 2780-157 Oeiras,
903 Portugal
- 904 **Marino F. A. Santos** – UCIBIO, Applied Molecular Biosciences
905 Unit, Departamento de Química, Faculdade de Ciências e
906 Tecnologia, Universidade Nova de Lisboa, 2829-516 Caparica,
907 Portugal
- 908 **Diana Gesto** – UCIBIO, Applied Molecular Biosciences Unit,
909 Departamento de Química, Faculdade de Ciências e Tecnologia,
910 Universidade Nova de Lisboa, 2829-516 Caparica, Portugal
- 911 **Bruno Guigliarelli** – Aix Marseille Université, CNRS, BIP,
912 Laboratoire de Bioénergétique et Ingénierie des Protéines,
913 Marseille 13402, France
- 914 **Teresa Santos-Silva** – UCIBIO, Applied Molecular Biosciences
915 Unit, Departamento de Química, Faculdade de Ciências e
916 Tecnologia, Universidade Nova de Lisboa, 2829-516 Caparica,
917 Portugal
- 918 Complete contact information is available at:
919 <https://pubs.acs.org/10.1021/acscatal.0c00086>
- 920 **Author Contributions**
921 ^{||}These authors contributed equally to this work.
- 922 **Notes**
923 The authors declare no competing financial interest.
- 924 **ACKNOWLEDGMENTS**
925 This work was financially supported by Fundação para a Ciência
926 e Tecnologia (Portugal) through fellowship SFRH/BD/
927 116515/2014 (to ARO), grant PTDC/BBB-EBB/2723/2014
928 (to I.A.C.P. and M.J.R.), and R&D units UID/Multi/04551/
929 2013 (Green-IT), LISBOA-01-0145-FEDER-007660 (MostMi-
930 cro) and (UID/Multi/04378/2019 (UCIBIO) cofunded by
931 FCT/MCTES and FEDER funds through COMPETE2020/
932 POCI. Funding from the European Union's Horizon 2020
933 research and innovation programme under grant agreement
934 number 810856 is also acknowledged. The authors are also
935 grateful to the EPR facilities available at the French EPR network
936 (IR CNRS 3443) and the Aix-Marseille University EPR centre.
- 937 **REFERENCES**
938 (1) Appel, A. M.; Bercaw, J. E.; Bocarsly, A. B.; Dobbek, H.; DuBois,
939 D. L.; Dupuis, M.; Ferry, J. G.; Fujita, E.; Hille, R.; Kenis, P. J. A.;
940 Kerfeld, C. A.; Morris, R. H.; Peden, C. H. F.; Portis, A. R.; Ragsdale, S.
941 W.; Rauchfuss, T. B.; Reek, J. N. H.; Seefeldt, L. C.; Thauer, R. K.;
942 Waldrop, G. L. Frontiers, Opportunities, and Challenges in
943 Biochemical and Chemical Catalysis of CO₂ Fixation. *Chem. Rev.*
944 **2013**, *113* (8), 6621–6658.
- 945 (2) Takeda, H.; Cometto, C.; Ishitani, O.; Robert, M. Electrons,
946 Photons, Protons and Earth-Abundant Metal Complexes for Molecular
947 Catalysis of CO₂ Reduction. *ACS Catal.* **2017**, *7* (1), 70–88.
- 948 (3) Shi, J.; Jiang, Y.; Jiang, Z.; Wang, X.; Wang, X.; Zhang, S.; Han, P.;
949 Yang, C. Enzymatic Conversion of Carbon Dioxide. *Chem. Soc. Rev.*
950 **2015**, *44* (17), 5981–6000.
- 951 (4) Schuchmann, K.; Müller, V. Autotrophy at the Thermodynamic
952 Limit of Life: A Model for Energy Conservation in Acetogenic Bacteria.
953 *Nat. Rev. Microbiol.* **2014**, *12* (12), 809–821.
- 954 (5) Cotton, C. A.; Edlich-Muth, C.; Bar-Even, A. Reinforcing Carbon
955 Fixation: CO₂ Reduction Replacing and Supporting Carboxylation.
956 *Curr. Opin. Biotechnol.* **2018**, *49*, 49–56.
- (6) Weiss, M. C.; Sousa, F. L.; Mrnjavac, N.; Neukirchen, S.; Roettger, 957
M.; Nelson-Sathi, S.; Martin, W. F. The Physiology and Habitat of the 958
Last Universal Common Ancestor. *Nat. Microbiol.* **2016**, *1* (9), 16116. 959
- (7) Yishai, O.; Lindner, S. N.; Gonzalez de la Cruz, J.; Tenenboim, H.; 960
Bar-Even, A. The Formate Bio-Economy. *Curr. Opin. Chem. Biol.* **2016**, 961
35, 1–9. 962
- (8) Singh, A. K.; Singh, S.; Kumar, A. Hydrogen Energy Future with 963
Formic Acid: A Renewable Chemical Hydrogen Storage System. *Catal.* 964
Sci. Technol. **2016**, *6* (1), 12–40. 965
- (9) Romão, M. J. Molybdenum and Tungsten Enzymes: A 966
Crystallographic and Mechanistic Overview. *Dalt. Trans.* **2009**, 967
No. 21, 4053. 968
- (10) Hartmann, T.; Schwanhold, N.; Leimkühler, S. Assembly and 969
Catalysis of Molybdenum or Tungsten-Containing Formate Dehydro- 970
genases from Bacteria. *Biochim. Biophys. Acta, Proteins Proteomics* **2015**, 971
1854 (9), 1090–1100. 972
- (11) Maia, L. B.; Moura, I.; Moura, J. J. G. Molybdenum and 973
Tungsten-Containing Formate Dehydrogenases: Aiming to Inspire a 974
Catalyst for Carbon Dioxide Utilization. *Inorg. Chim. Acta* **2017**, *455*, 975
350–363. 976
- (12) Niks, D.; Hille, R. Molybdenum- and Tungsten-Containing 977
Formate Dehydrogenases and Formylmethanofuran Dehydrogenases: 978
Structure, Mechanism, and Cofactor Insertion. *Protein Sci.* **2019**, *28* 979
(1), 111–122. 980
- (13) Reda, T.; Plugge, C. M.; Abram, N. J.; Hirst, J. Reversible 981
Interconversion of Carbon Dioxide and Formate by an Electroactive 982
Enzyme. *Proc. Natl. Acad. Sci. U. S. A.* **2008**, *105* (31), 10654–10658. 983
- (14) Schuchmann, K.; Müller, V. Direct and Reversible Hydro- 984
genation of CO₂ to Formate by a Bacterial Carbon Dioxide Reductase. 985
Science **2013**, *342* (6164), 1382–1385. 986
- (15) Maia, L. B.; Fonseca, L.; Moura, I.; Moura, J. J. G. Reduction of 987
Carbon Dioxide by a Molybdenum-Containing Formate Dehydrogen- 988
ase: A Kinetic and Mechanistic Study. *J. Am. Chem. Soc.* **2016**, *138* (28), 989
8834–8846. 990
- (16) Schwarz, F. M.; Schuchmann, K.; Müller, V. Hydrogenation of 991
CO₂ at Ambient Pressure Catalyzed by a Highly Active Thermostable 992
Biocatalyst. *Biotechnol. Biofuels* **2018**, *11* (1), 237. 993
- (17) Hartmann, T.; Leimkühler, S. The Oxygen-Tolerant and NAD⁺- 994
Dependent Formate Dehydrogenase from *Rhodobacter Capsulatus* Is 995
Able to Catalyze the Reduction of CO₂ to Formate. *FEBS J.* **2013**, *280* 996
(23), 6083–6096. 997
- (18) Yu, X.; Niks, D.; Mulchandani, A.; Hille, R. Efficient Reduction of 998
CO₂ by the Molybdenum-Containing Formate Dehydrogenase from 999
Cupriavidus Necator (Ralstonia Eutropha). *J. Biol. Chem.* **2017**, *292* (41), 1000
16872–16879. 1001
- (19) Thomé, R.; Gust, A.; Toci, R.; Mendel, R.; Bittner, F.; Magalon, 1002
A.; Walburger, A. A Sulfurtransferase Is Essential for Activity of 1003
Formate Dehydrogenases in *Escherichia Coli*. *J. Biol. Chem.* **2012**, *287* 1004
(7), 4671–4678. 1005
- (20) Arnoux, P.; Ruppelt, C.; Oudouhou, F.; Lavergne, J.; Siponen, M. 1006
I.; Toci, R.; Mendel, R. R.; Bittner, F.; Pignol, D.; Magalon, A.; 1007
Walburger, A. Sulphur Shuttling across a Chaperone during 1008
Molybdenum Cofactor Maturation. *Nat. Commun.* **2015**, *6* (1), 6148. 1009
- (21) Schrapers, P.; Hartmann, T.; Kositzki, R.; Dau, H.; Reschke, S.; 1010
Schulzke, C.; Leimkühler, S.; Haumann, M. Sulfido and Cysteine 1011
Ligation Changes at the Molybdenum Cofactor during Substrate 1012
Conversion by Formate Dehydrogenase (FDH) from *Rhodobacter* 1013
Capsulatus. *Inorg. Chem.* **2015**, *54* (7), 3260–3271. 1014
- (22) Robinson, W. E.; Bassegoda, A.; Reisner, E.; Hirst, J. Oxidation- 1015
State-Dependent Binding Properties of the Active Site in a Mo- 1016
Containing Formate Dehydrogenase. *J. Am. Chem. Soc.* **2017**, *139* (29), 1017
9927–9936. 1018
- (23) Raaijmakers, H. C. A.; Romão, M. J. Formate-Reduced *E. Coli* 1019
Formate Dehydrogenase H: The Reinterpretation of the Crystal 1020
Structure Suggests a New Reaction Mechanism. *JBIC, J. Biol. Inorg.* 1021
Chem. **2006**, *11* (7), 849–854. 1022
- (24) Grimaldi, S.; Schoepp-Cothenet, B.; Ceccaldi, P.; Guigliarelli, B.; 1023
Magalon, A. The Prokaryotic Mo/W-BisPGD Enzymes Family: A 1024

- 1025 Catalytic Workhorse in Bioenergetics. *Biochim. Biophys. Acta, Bioenerg.* **2013**, *1827* (8–9), 1048–1085.
- 1026 (25) Mota, C. S.; Rivas, M. G.; Brondino, C. D.; Moura, I.; Moura, J. J. G.; Gonzalez, P. J.; Cerqueira, N. M. F. S. A. The Mechanism of Formate Oxidation by Metal-Dependent Formate Dehydrogenases. *JBIC, J. Biol. Inorg. Chem.* **2011**, *16* (8), 1255–1268.
- 1031 (26) Tiberti, M.; Papaleo, E.; Russo, N.; De Gioia, L.; Zampella, G. Evidence for the Formation of a Mo–H Intermediate in the Catalytic Cycle of Formate Dehydrogenase. *Inorg. Chem.* **2012**, *51* (15), 8331–8339.
- 1035 (27) Cerqueira, N. M. F. S. A.; Fernandes, P. A.; Gonzalez, P. J.; Moura, J. J. G.; Ramos, M. J. The Sulfur Shift: An Activation Mechanism for Periplasmic Nitrate Reductase and Formate Dehydrogenase. *Inorg. Chem.* **2013**, *52* (19), 10766–10772.
- 1039 (28) Hartmann, T.; Schrapers, P.; Utesch, T.; Nimtz, M.; Rippers, Y.; Dau, H.; Mroginski, M. A.; Haumann, M.; Leimkuhler, S. The Molybdenum Active Site of Formate Dehydrogenase Is Capable of Catalyzing C–H Bond Cleavage and Oxygen Atom Transfer Reactions. *Biochemistry* **2016**, *55* (16), 2381–2389.
- 1044 (29) Niks, D.; Duvvuru, J.; Escalona, M.; Hille, R. Spectroscopic and Kinetic Properties of the Molybdenum-Containing, NAD⁺-Dependent Formate Dehydrogenase from *Ralstonia Eutropha*. *J. Biol. Chem.* **2016**, *291* (3), 1162–1174.
- 1048 (30) Dong, G.; Ryde, U. Reaction Mechanism of Formate Dehydrogenase Studied by Computational Methods. *JBIC, J. Biol. Inorg. Chem.* **2018**, *23* (8), 1243–1254.
- 1051 (31) Boyington, J. C.; Gladyshev, V. N.; Khangulov, S. V.; Stadtman, T. C.; Sun, P. D. Crystal Structure of Formate Dehydrogenase H: Catalysis Involving Mo, Molybdopterin, Selenocysteine, and an Fe₄S₄ Cluster. *Science* **1997**, *275* (5304), 1305–1308.
- 1055 (32) Jormakka, M.; Tornroth, S.; Byrne, B.; Iwata, S. Molecular Basis of Proton Motive Force Generation: Structure of Formate Dehydrogenase-N. *Science* **2002**, *295* (5561), 1863–8.
- 1058 (33) Raaijmakers, H.; Macieira, S.; Dias, J. M.; Teixeira, S.; Bursakov, S.; Huber, R.; Moura, J. J. G.; Moura, I.; Romao, M. J. Gene Sequence and the 1.8 Å Crystal Structure of the Tungsten-Containing Formate Dehydrogenase from *Desulfovibrio gigas*. *Structure* **2002**, *10* (9), 1261–1272.
- 1063 (34) George, G. N.; Colangelo, C. M.; Dong, J.; Scott, R.; Khangulov, S. V.; Gladyshev, V. N.; Stadtman, T. C. X-Ray Absorption Spectroscopy of the Molybdenum Site of *Escherichia coli* Formate Dehydrogenase. *J. Am. Chem. Soc.* **1998**, *120*, 1267–1273.
- 1067 (35) George, G. N.; Costa, C.; Moura, J. J. G.; Moura, I. Observation of Ligand-Based Redox Chemistry at the Active Site of a Molybdenum Enzyme. *J. Am. Chem. Soc.* **1999**, *121*, 2625–2626.
- 1070 (36) Khangulov, S. V.; Gladyshev, V. N.; Dismukes, G. C.; Stadtman, T. C. Selenium-Containing Formate Dehydrogenase H from *Escherichia coli*: A Molybdopterin Enzyme That Catalyzes Formate Oxidation without Oxygen Transfer. *Biochemistry* **1998**, *37* (10), 3518–3528.
- 1075 (37) Maia, L. B.; Moura, I.; Moura, J. J. G. *EPR Spectroscopy on Mononuclear Molybdenum-Containing Enzymes*; Springer: Cham, 2017; pp 55–101 DOI: 10.1007/978-3-319-59100-1_4.
- 1078 (38) Grimaldi, S.; Biaso, F.; Burlat, B.; Guigliarelli, B. Electron Paramagnetic Resonance Studies of Molybdenum Enzymes. In *Molybdenum and Tungsten Enzymes: Spectroscopic and Theoretical Investigations*; Hille, R., Schulzke, C., Kirk, M. L., Eds.; American Chemical Society, 2016; pp 68–120.
- 1083 (39) Axley, M. J.; Bock, A.; Stadtman, T. C. Catalytic Properties of an *Escherichia coli* Formate Dehydrogenase Mutant in Which Sulfur Replaces Selenium. *Proc. Natl. Acad. Sci. U. S. A.* **1991**, *88* (19), 8450–8454.
- 1087 (40) Stams, A. J.; Plugge, C. M. Electron Transfer in Syntrophic Communities of Anaerobic Bacteria and Archaea. *Nat. Rev. Microbiol.* **2009**, *7* (8), 568–577.
- 1090 (41) Plugge, C. M.; Zhang, W.; Scholten, J. C.; Stams, A. J. Metabolic Flexibility of Sulfate-Reducing Bacteria. *Front. Microbiol.* **2011**, *2*, 81.
- 1092 (42) de Bok, F. A. M.; Hagedoorn, P. L.; Silva, P. J.; Hagen, W. R.; Schiltz, E.; Fritsche, K.; Stams, A. J. M. Two W-Containing Formate Dehydrogenases (CO₂-Reductases) Involved in Syntrophic Propionate Oxidation by *Syntrophobacter fumaroxidans*. *Eur. J. Biochem.* **2003**, *270* (11), 2476–2485.
- 1096 (43) da Silva, S. M.; Voordouw, J.; Leitão, C.; Martins, M.; Voordouw, G.; Pereira, I. A. C. Function of Formate Dehydrogenases in *Desulfovibrio vulgaris* Hildenborough Energy Metabolism. *Microbiology (London, U. K.)* **2013**, *159* (8), 1760–1769.
- 1100 (44) da Silva, S. M.; Pimentel, C.; Valente, F. M. A.; Rodrigues-Pousada, C.; Pereira, I. A. C. Tungsten and Molybdenum Regulation of Formate Dehydrogenase Expression in *Desulfovibrio vulgaris* Hildenborough. *J. Bacteriol.* **2011**, *193* (12), 2909–2916.
- 1104 (45) Keller, K. L.; Wall, J. D.; Chhabra, S. Methods for Engineering Sulfate Reducing Bacteria of the Genus *Desulfovibrio*. *Methods Enzymol.* **2011**, *497*, 503–517.
- 1107 (46) Niks, D.; Hille, R. Reductive Activation of CO₂ by Formate Dehydrogenases. *Methods Enzymol.* **2018**, *613*, 277–295.
- 1109 (47) Almendra, M. J.; Brondino, C. D.; Gavel, O.; Pereira, A. S.; Tavares, P.; Bursakov, S.; Duarte, R.; Caldeira, J.; Moura, J. J. G.; Moura, I. Purification and Characterization of a Tungsten-Containing Formate Dehydrogenase from *Desulfovibrio gigas*. *Biochemistry* **1999**, *38* (49), 16366–16372.
- 1114 (48) Bassegoda, A.; Madden, C.; Wakerley, D. W.; Reisner, E.; Hirst, J. Reversible Interconversion of CO₂ and Formate by a Molybdenum-Containing Formate Dehydrogenase. *J. Am. Chem. Soc.* **2014**, *136*, 15473–15476.
- 1118 (49) Sokol, K. P.; Robinson, W. E.; Oliveira, A. R.; Warnan, J.; Nowaczyk, M. M.; Ruff, A.; Pereira, I. A. C.; Reisner, E. Photoreduction of CO₂ with a Formate Dehydrogenase Driven by Photosystem II Using a Semi-Artificial Z-Scheme Architecture. *J. Am. Chem. Soc.* **2018**, *140* (48), 16418–16422.
- 1123 (50) Miller, M.; Robinson, W. E.; Oliveira, A. R.; Heidary, N.; Kornienko, N.; Warnan, J.; Pereira, I.; Reisner, E. Interfacing Formate Dehydrogenase with Metal Oxides for Reversible Electrocatalysis and Solar-Driven Reduction of Carbon Dioxide. *Angew. Chem.* **2019**, *131* (14), 4649–4653.
- 1128 (51) Caillet-Saguy, C.; Turano, P.; Piccioli, M.; Lukat-Rodgers, G. S.; Czjzek, M.; Guigliarelli, B.; Izadi-Pruneyre, N.; Rodgers, K. R.; Delepierre, M.; Lecroisey, A. Deciphering the Structural Role of Histidine 83 for Heme Binding in Hemophore HasA. *J. Biol. Chem.* **2008**, *283*, 5960–5970.
- 1133 (52) Duval, S.; Santini, J. M.; Lemaire, D.; Chaspoul, F.; Russell, M. J.; Grimaldi, S.; Nitschke, W.; Schoepp-Cothenet, B. The H-Bond Network Surrounding the Pyranopterins Modulates Redox Cooperativity in the Molybdenum-BisPGD Cofactor in Arsenite Oxidase. *Biochim. Biophys. Acta, Bioenerg.* **2016**, *1857* (9), 1353–1362.
- 1138 (53) Wu, S. Y.; Rothery, R. A.; Weiner, J. H. Pyranopterin Coordination Controls Molybdenum Electrochemistry in *Escherichia coli* Nitrate Reductase. *J. Biol. Chem.* **2015**, *290* (41), 25164–25173.
- 1141 (54) Rothery, R. A.; Weiner, J. H. Shifting the Metallocentric Molybdoenzyme Paradigm: The Importance of Pyranopterin Coordination. *JBIC, J. Biol. Inorg. Chem.* **2015**, *20*, 349–372.
- 1144 (55) Magalon, A.; Ceccaldi, P.; Schoepp-Cothenet, B. The Prokaryotic Mo/W-BisPGD Enzymes Family. In *RSC Metallobiology—Molybdenum and Tungsten Enzymes: Biochemistry*; Hille, R., Schulzke, C., Kirk, M. L., Eds.; 2017; Vol. 2017, pp 143–191 DOI: 10.1039/9781782623915-00143.
- 1149 (56) Zorn, M.; Ihling, C. H.; Golbik, R.; Sawers, R. G.; Sinz, A. Selective SelC-Independent Selenocysteine Incorporation into Formate Dehydrogenases. *PLoS One* **2013**, *8* (4), No. e61913.
- 1152 (57) Ma, S.; Caprioli, R. M.; Hill, K. E.; Burk, R. F. Loss of Selenium from Selenoproteins: Conversion of Selenocysteine to Dehydroalanine in Vitro. *J. Am. Soc. Mass Spectrom.* **2003**, *14* (6), 593–600.
- 1155 (58) Marques, M. C.; Tapia, C.; Gutiérrez-Sanz, O.; Ramos, A. R.; Keller, K. L.; Wall, J. D.; De Lacey, A. L.; Matias, P. M.; Pereira, I. A. C. The Direct Role of Selenocysteine in [NiFeSe] Hydrogenase Maturation and Catalysis. *Nat. Chem. Biol.* **2017**, *13* (5), 544.
- 1159 (59) Smee, J. J.; Goodman, D. C.; Reibenspies, J. H.; Darensbourg, M. Y. Models for Terminal Ni(S-Cysteine) Modification in [NiFe]-

- 1162 Hydrogenases by Iodoacetamide and Iodoacetate. *Eur. J. Inorg. Chem.*
1163 **1999**, 1999 (3), 539–546.
- 1164 (60) Rothery, R. A.; Stein, B.; Solomonson, M.; Kirk, M. L.; Weiner, J.
1165 H. Pyranopterin Conformation Defines the Function of Molybdenum
1166 and Tungsten Enzymes. *Proc. Natl. Acad. Sci. U. S. A.* **2012**, 109 (37),
1167 14773–14778.
- 1168 (61) Gisewhite, D. R.; Yang, J.; Williams, B. R.; Esmail, A.; Stein, B.;
1169 Kirk, M. L.; Burgmayer, S. J. N. Implications of Pyran Cyclization and
1170 Pterin Conformation on Oxidized Forms of the Molybdenum Cofactor.
1171 *J. Am. Chem. Soc.* **2018**, 140, 12808–12818.
- 1172 (62) Jacques, J. G. J.; Fourmond, V.; Arnoux, P.; Sabaty, M.; Etienne,
1173 E.; Grosse, S.; Biaso, F.; Bertrand, P.; Pignol, D.; Léger, C.; Guigliarelli,
1174 B.; Burlat, B. Reductive Activation in Periplasmic Nitrate Reductase
1175 Involves Chemical Modifications of the Mo-Cofactor beyond the First
1176 Coordination Sphere of the Metal Ion. *Biochim. Biophys. Acta, Bioenerg.*
1177 **2014**, 1837, 277–286.
- 1178 (63) Moura, J. J. G.; Brondino, C. D.; Trincão, J.; Romão, M. J. Mo
1179 and W Bis-MGD Enzymes: Nitrate Reductases and Formate
1180 Dehydrogenases. *JBIC, J. Biol. Inorg. Chem.* **2004**, 9 (7), 791–799.
- 1181 (64) McCarthy, A. A.; Barrett, R.; Beteva, A.; Caserotto, H.; Dobias,
1182 F.; Felisaz, F.; Giraud, T.; Guijarro, M.; Janocha, R.; Khadrouché, A.;
1183 et al. ID30B – a Versatile Beamline for Macromolecular Crystallog-
1184 raphy Experiments at the ESRF. *J. Synchrotron Radiat.* **2018**, 25 (4),
1185 1249–1260.
- 1186 (65) Kabsch, W. XDS. *Acta Crystallogr., Sect. D: Biol. Crystallogr.* **2010**,
1187 66, 125–132.
- 1188 (66) Evans, P. R.; Murshudov, G. N. How Good Are My Data and
1189 What Is the Resolution? *Acta Crystallogr., Sect. D: Biol. Crystallogr.* **2013**,
1190 69, 1204–14.
- 1191 (67) McCoy, A. J.; Grosse-Kunstleve, R. W.; Adams, P. D.; Winn, M.
1192 D.; Storoni, L. C.; Read, R. J. Phaser Crystallographic Software. *J. Appl.*
1193 *Crystallogr.* **2007**, 40, 658–674.
- 1194 (68) Stein, N. CHAINSAW: A Program for Mutating Pdb Files Used
1195 as Templates in Molecular Replacement. *J. Appl. Crystallogr.* **2008**, 41,
1196 641–643.
- 1197 (69) Emsley, P.; Lohkamp, B.; Scott, W. G.; Cowtan, K. Features and
1198 Development of Coot. *Acta Crystallogr., Sect. D: Biol. Crystallogr.* **2010**,
1199 66, 486–501.
- 1200 (70) Afonine, P. V.; Grosse-Kunstleve, R. W.; Echols, N.; Headd, J. J.;
1201 Moriarty, N. W.; Mustyakimov, M.; Terwilliger, T. C.; Urzhumtsev, A.;
1202 Zwart, P. H.; Adams, P. D. Towards Automated Crystallographic
1203 Structure Refinement with Phenix. Refine. *Acta Crystallogr., Sect. D:*
1204 *Biol. Crystallogr.* **2012**, 68, 352–364.
- 1205 (71) Chovancova, E.; Pavelka, A.; Benes, P.; Strnad, O.; Brezovsky, J.;
1206 Kozlikova, B.; Gora, A.; Sustr, V.; Klvana, M.; Medek, P.;
1207 Biedermannova, L.; Sochor, J.; Damborsky, J. CAVER 3.0: A Tool
1208 for the Analysis of Transport Pathways in Dynamic Protein Structures.
1209 *PLoS Comput. Biol.* **2012**, 8, No. e1002708.
- 1210 (72) Finn, R. D.; Clements, J.; Eddy, S. R. HMMER Web Server:
1211 Interactive Sequence Similarity Searching. *Nucleic Acids Res.* **2011**, 39,
1212 W29–W37.
- 1213 (73) Huang, Y.; Niu, B.; Gao, Y.; Fu, L.; Li, W. CD-HIT Suite: A Web
1214 Server for Clustering and Comparing Biological Sequences. *Bio-*
1215 *informatics* **2010**, 26 (5), 680–682.
- 1216 (74) Katoh, K.; Misawa, K.; Kuma, K.; Miyata, T. MAFFT: A Novel
1217 Method for Rapid Multiple Sequence Alignment Based on Fast Fourier
1218 Transform. *Nucleic Acids Res.* **2002**, 30 (14), 3059–3066.
- 1219 (75) Kumar, S.; Stecher, G.; Li, M.; Nnyaz, C.; Tamura, K. MEGA X:
1220 Molecular Evolutionary Genetics Analysis across Computing Plat-
1221 forms. *Mol. Biol. Evol.* **2018**, 35 (6), 1547–1549.
- 1222 (76) Waterhouse, A. M.; Procter, J. B.; Martin, D. M. A.; Clamp, M.;
1223 Barton, G. J. Jalview Version 2—a Multiple Sequence Alignment Editor
1224 and Analysis Workbench. *Bioinformatics* **2009**, 25 (9), 1189–1191.